Rational design of hollow rice-grained α-Fe$_2$O$_3$/carbon nanofibers with optimized impedance matching for electromagnetic wave absorption enhanced

Jingshen Xu[1], Na Lu[1], Mengwei Yuan[2], and Genban Sun[1,2] (✉)

[1] *Beijing Key Laboratory of Energy Conversion and Storage Materials, College of Chemistry, Beijing Normal University, Beijing 100875, China*
[2] *Center for Advanced Materials Research, Beijing Normal University, Zhuhai 519087, China*

ABSTRACT

Electromagnetic wave absorption materials are widely used in electronic equipment and military fields. However, high cost and complex preparation processes become a major obstacle in promoting popularization in the civil field. To solve the problems above, researchers have made great efforts to develop Fe-based carbon composites. However, most of the typical composites require a high filling ratio while achieving excellent properties. Therefore, in this study, carbon nanofibers (CNFs) combined with the hollow rice-grained α-Fe$_2$O$_3$ nanoparticles were prepared by the *in-situ* transformation method. The rational microstructure design provided a solution for reducing the filling ratio, optimizing impedance matching, and improving electromagnetic wave absorption performance. The strong reflection loss value (−38.1 dB) and broad effective absorption bandwidth (4.6 GHz) for Fe$_2$O$_3$/CNFs composites were achieved with a low filling ratio (20 wt.%), and the analysis of electromagnetic parameters validated that the microstructure of Fe$_2$O$_3$/CNFs plays a crucial role in the performance improvement. With the optimized impedance matching and simple preparation method, Fe$_2$O$_3$/CNFs have broad application prospects in electromagnetic wave absorption.

KEYWORDS

electromagnetic wave absorption, Fe-based, carbon nanofibers, impedance matching

1   Introduction

The advent of the 5G era further intensifies our demands for electromagnetic wave (EMW) absorption materials [1]. Dealing with EMW pollution caused by a large number of electronic devices [2, 3] and the urgent requirement for radar stealth technology in the military field [4–7], it needs to accelerate the development of new high-efficiency EMW absorbing materials. However, up to now, simple synthesis methods, controllable product morphology, inexpensive raw materials, and excellent EMW absorption performance remain an urgent problem to be solved, which badly limits the usage of EMW absorption materials [8–11].

Now, researchers pay more attention to magnetic materials with the simple manufacturing process and can easily realize rational microstructure design for improving EMW absorption abilities. These advantages make ferrite materials become a hotspot. Ferrite is a kind of double-compound dielectric material, and the resistivity of ferrite is much bigger than single metal or alloy magnetic materials [12]. Liu et al. [11] prepared the urchin-like Fe/α-Fe$_2$O$_3$ nanocomposite. Firstly, using the geometric effect brought by the isotropic antenna shape, the material can obtain multiple reflection paths which make the EMW to be effectively attenuated. Secondly, the presence of Fe$_2$O$_3$ crystals can effectively improve the resistivity of the material and reduce the polarization degree of the space charge. Zhang et al. [13] constructed holey γ-Fe$_2$O$_3$ nanosheets. The increased surface area not only offers more chance to construct oxygen vacancy and polarization centers, but also extends the propagation path of EMW inside the material. The increased electrical conductivity and the strengthened conduction loss mechanism can improve the impedance matching ability and enhance EMW absorption performance. For a porous α-Fe$_2$O$_3$ EMW absorber, Cheng et al. [14] explored the effect of nano-structure on EMW absorption performance and found that reflection loss (RL) value can be effectively reduced due to the rough surface of the porous structure, which can increase multiple reflection paths and scattering intensity. The above work shows that building porous or enriching reflection paths is essential to the improvement of material morphology, which plays as a key factor in EMW energy dissipation.

However, dielectric materials (graphene [15, 16], carbon nanotubes [17, 18], carbon fiber [19, 20], and silicon carbide [21]) or magnetic materials (Fe- [22], Co- [23], and Ni-based [24]) used independently are difficult to meet the high standard of low thickness, lightweight, strong RL, and broad effective absorption bandwidth (EAB) [4]. The composite materials can provide good dielectric properties and excellent magnetic loss performance with a low doping mass [25, 26], which has become an efficient solution to improve impedance matching and enrich the loss mechanism. Electrospinning technology has low cost, high yield, high aspect ratio, and excellent mechanical stability [27, 28]. Luo et

al. [29] anchored ultra-small Fe_3O_4 on the surface of carbon nanofibers (CNFs) in a highly dispersed manner, which could provide rich interface structures, resulting in strong interface polarization and polarization lags. Besides, the three-dimensional (3D) network and the porous structure provide multi-reflections which lead to more energy loss. In our previous work, we constructed macro-porous Fe_3C/N-C CNFs and $CoFe_2O_4/CNFs$ by electro-spinning technology, respectively. SiO_2 microsphere was used as the template to construct irregular large holes on the surface of CNFs to reduce the material density and enhance the multiple reflection loss. Experiment results show that when the doping mass was 10 wt.%, the EAB reached 4.6 GHz and the RL_{min} was −22.1 dB [30, 31].

Inspired by the previous studies, we would like to set microstructural effects as an entry point for exploring EMW absorption performance improvement. As shown in Fig. 1, we selected the *in-situ* transformation method to synthesize FeOOH/CNFs as the precursor in a constant temperature water bath and then get the $Fe_2O_3/CNFs$ by calcination, avoiding the high temperature/pressure experimental conditions as much as possible. α-Fe_2O_3, as a paramagnetic material, only provides poor magnetic loss ability, which ensures that the composite performance enhancement is not affected by the magnetic loss material, but depends more on the advantages brought by the microstructure. By characterizing the EMW absorbing properties of composite materials with different nanoparticle load ratios, we find that the rational design of microstructure successfully makes up for the weak magnetic loss ability and realizes the EMW absorption performance enhancement. When the filling ratio between the $Fe_2O_3/CNFs$ and the paraffin is 2:8, $Fe_2O_3/CNFs$-4 has the best EMW absorption properties. With 2 mm thickness, the RL_{min} is −29.8 dB and the EAB is 4.6 GHz. When the thickness increases to 2.3 mm, the RL_{min} is −38.1 dB with 4 GHz bandwidth, which is close to even surpassing most relevant composite materials.

2 Results and discussion

In Fig. 2(a), the $Fe_2O_3/CNFs$ samples show obvious peaks at 24.1°, 33.2°, 35.6°, 49.5°, 54.1°, and 62.4°, corresponding to (012), (104), (110), (024), (116), and (214) of the α-Fe_2O_3, respectively (JCPDS card No. 33-0664). Compared with Fig. S3 in the Electronic Supplementary Material (ESM), the characteristic peaks of (110) and (310) at 11.8° and 26.7° disappear, proving that all FeO(OH)

in the composites has been transformed into α-Fe_2O_3. According to the X-ray diffraction (XRD) results above, the $Fe_2O_3/CNFs$ are successfully prepared by the *in-situ* transformation method.

Figure 2(b) and Fig. S4 in the ESM show the surface composition of the $Fe_2O_3/CNFs$ collected by X-ray photoelectron spectroscopy (XPS). The XPS peaks of C 1s, Fe 2p, and O 1s for $Fe_2O_3/CNFs$-4 composites can be found in Fig. 2(b_1), respectively. The C 1s spectrum of the composite material in 284.8, 286.2, and 288.3 eV (Fig. 2(b_2)) could be assigned to C–C, C–O, and C–N bonds, respectively [31]. Figure 2(b_3) presents the Fe 2p in $Fe_2O_3/CNFs$, with the obvious satellite peaks at 718.8 and 733.6 eV, suggesting the presence of Fe^{3+} [31–33]. The Fe $2p_{3/2}$ (711.9 eV) and Fe $2p_{1/2}$ (725.0 eV) for Fe_2O_3 broaden and shift to high binding energy due to the appearance of Fe^{2+} on the surface [33]. The coexistence of Fe^{3+} and Fe^{2+} states may be caused by a small amount of Fe^{3+} directly contacted with active carbon being reduced to Fe^{2+} under Ar atmosphere and high temperature [34]. However, due to the short calcination time and low calcination temperature, the content of Fe^{2+} is not high enough, there is no other phase generated in XRD, and the main composition is α-Fe_2O_3 [35]. Figure 2(b_4) shows the O 1s spectra of $Fe_2O_3/CNFs$-4 material, in which the binding energy of lattice oxygen, oxygen defect, and surface adsorbed oxygen is around 530.0, 531.5, and 533.3 eV, respectively, further supporting the formation of α-Fe_2O_3.

The Raman spectra of $Fe_2O_3/CNFs$ and pure CNFs materials are shown in Fig. 2(c). The D and G bands of the carbon usually show two broad peaks at 1,332 and 1,580 cm^{-1} [36], and the I_D/I_G value is related to the disorder degree of the carbon material. Compared with pure CNFs, the I_D/I_G value of the composite material generally increases from 0.99 to 1.29, indicating that the number of sp^2 hybrid carbon atoms and the defects in composite materials is more than in pure CNFs. The more Fe_2O_3 nanoparticles there are, the more defects, which act as polarization centers in the changing electromagnetic field, will be caused. Figure S5 in the ESM shows the thermo gravimetric analysis (TGA) curve of the $Fe_2O_3/CNFs$. Due to the decomposition of CNFs in the air, the mass of the material remains stable after 600 °C, so we can obtain the content of Fe_2O_3 in the different composite materials. Figure S5 in the ESM shows the mass loss of 60.44%, 50.71%, and 40.30%, corresponding to $Fe_2O_3/CNFs$-2, $Fe_2O_3/CNFs$-4, and $Fe_2O_3/CNFs$-6, respectively. The content of the composite material changes radiantly, which is positively correlated with the initial addition proportion of $FeCl_3$. However,
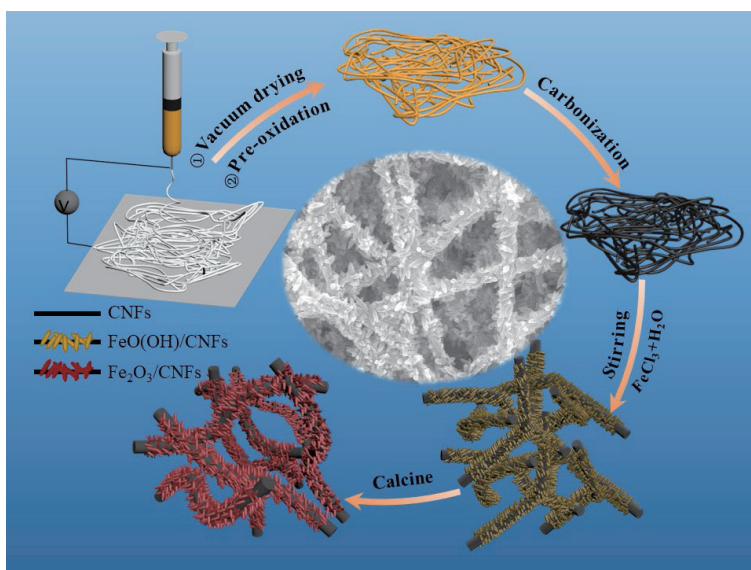

Figure 1 Schematic diagram of the strategy to prepare α-$Fe_2O_3/CNFs$

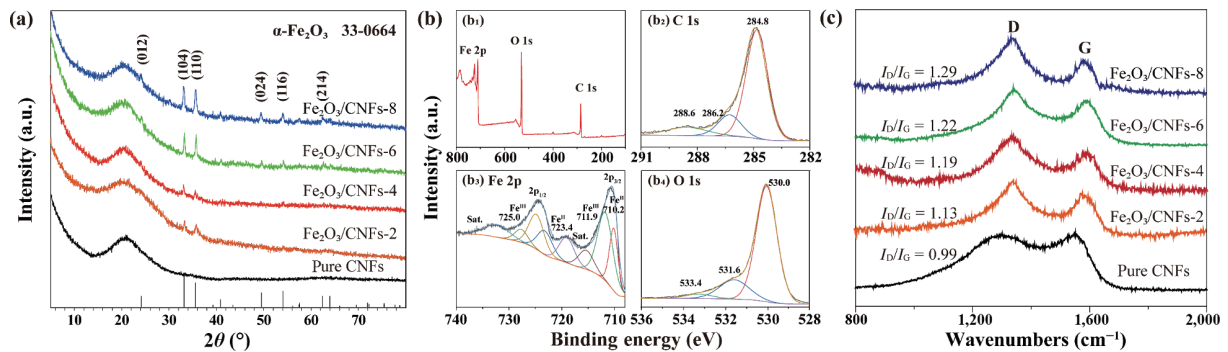**Figure 2** (a) XRD patterns of Fe$_2$O$_3$/CNFs and pure CNFs, (b) XPS spectra of the Fe$_2$O$_3$/CNFs-4, and (c) Raman shift of Fe$_2$O$_3$/CNFs and pure CNFs.

the mass loss of Fe$_2$O$_3$/CNFs-8 is 39.67%, which is close to Fe$_2$O$_3$/CNFs-6, indicating that the load limit of CNFs has been reached.

Figures 3(a$_1$)–3(d$_2$) show the scanning electron microscopy (SEM) images of different composite materials. Compared with Figs. S1 and S6 in the ESM, Fe$_2$O$_3$ nanoparticles packed on the CNFs surface tightly and densely. After calcination, there is no agglomeration or morphology collapse. The structure morphology is maintained, and the size distribution is uniform, about 200 nm. It can also be observed from Fig. S7 in the ESM that the Fe$_2$O$_3$ nanoparticles show hollow structures based on maintaining their rice-grained morphology, in which thickness is about 10 nm. In general, hydrolysis occurs on the surface first, and then inside. The Kirkendall effect will occur if the hydrolysis and diffusion rate of the inner (core) is faster than the outer (shell) [37]. The H$^+$ or OH$^-$ ions (also known as H$_2$O) escape from their original positions in the lattice to the surface of the nanoparticle, then form a water molecular membrane and rapidly evaporate, resulting in the formation of vacancies in the crystal, and some edges merge into voids [37]. With the further increase of the temperature in the next stage, the relative migration of other ions will be caused, and the diffusion to the cavity will gradually reduce or even eliminate [38]. Therefore, the Fe$_2$O$_3$ nanoparticles with hollow structures can be found in Fig. S7 in the ESM.

Figures 3(e) and 3(f) are transmission electron microscopy (TEM) images of Fe$_2$O$_3$/CNFs-4, which clearly show that Fe$_2$O$_3$ nanoparticles are uniformly loaded on the surface of CNFs and there is no agglomeration or morphological collapse between the nanoparticles. As marked in Figs. 3(e) and 3(f), the hollow core–shell structure of Fe$_2$O$_3$ nanoparticles can be seen clearly, and the shell thickness is about 10 nm. The measured lattice spaces in Fig. 3(g) are 0.36 and 0.27 nm, which correspond with the (012) and (104) planes of Fe$_2$O$_3$. In addition, the clear diffraction rings can be assigned to the (018), (024), and (006) crystal planes of Fe$_2$O$_3$. The elemental mapping diagram of Fe$_2$O$_3$/CNFs is consistent with Fig. 3(e), the elements C, O, and Fe coexist in Fe$_2$O$_3$/CNFs, and the mass percentage of C elements is 50.23%, which matches well with the TGA result of Fe$_2$O$_3$/CNFs-4 showed in Fig. S5 in the ESM, proving that Fe$_2$O$_3$ is uniformly dispersed on the CNFs.

The RL curves of FeO(OH)/CNFs and Fe$_2$O$_3$/CNFs (20 wt.%) in 1–18 GHz are shown in Fig. 4, and Figs. S8 and S9 in the ESM. To better compare the properties of FeOOH/CNFs and Fe$_2$O$_3$/CNFs, a 20 wt.% filling ratio and 2 mm thickness condition were stipulated in Figs. 4(a) and 4(b). Compared with the pure CNFs, the EMW absorption performance of FeO(OH)/CNFs and Fe$_2$O$_3$/CNFs series is both significantly enhanced. However, FeOOH is easy to decompose and deteriorate, and the product

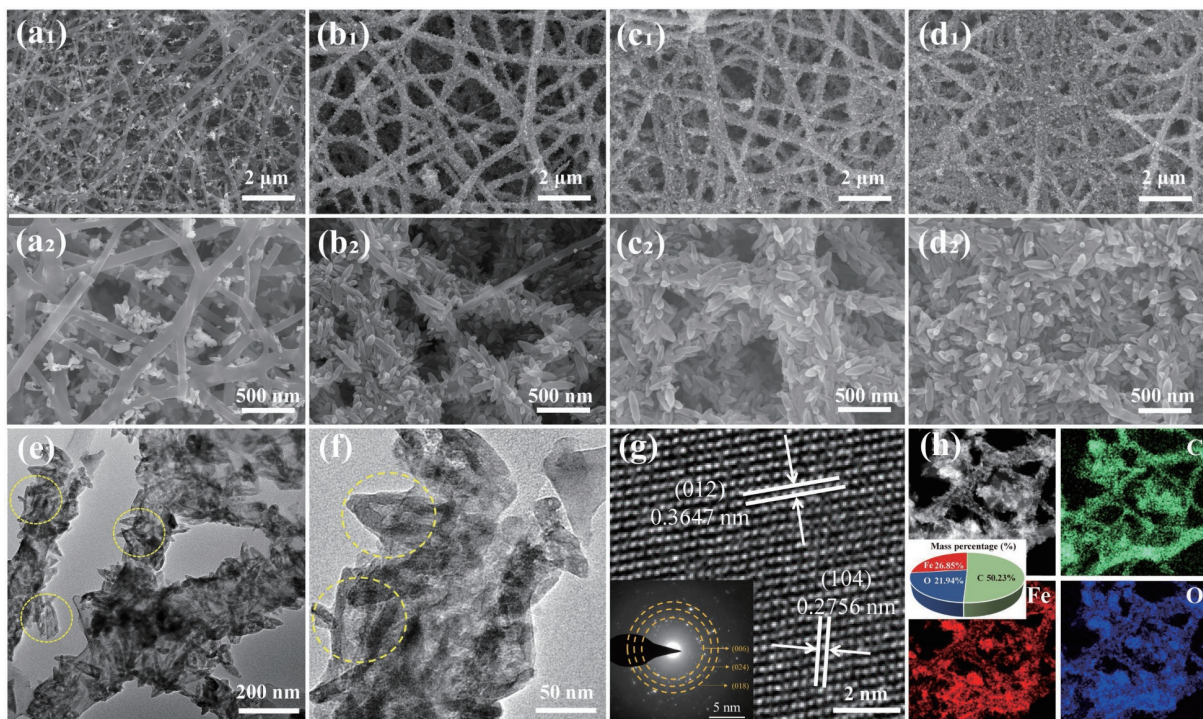**Figure 3** SEM images of (a$_1$, a$_2$) Fe$_2$O$_3$/CNFs-2, (b$_1$, b$_2$) Fe$_2$O$_3$/CNFs-4, (c$_1$, c$_2$) Fe$_2$O$_3$/CNFs-6, and (d$_1$, d$_2$) Fe$_2$O$_3$/CNFs-8. (e, f) TEM images, (g) HRTEM and SAED image, and (h) EDX mapping images of Fe$_2$O$_3$/CNFs-4.
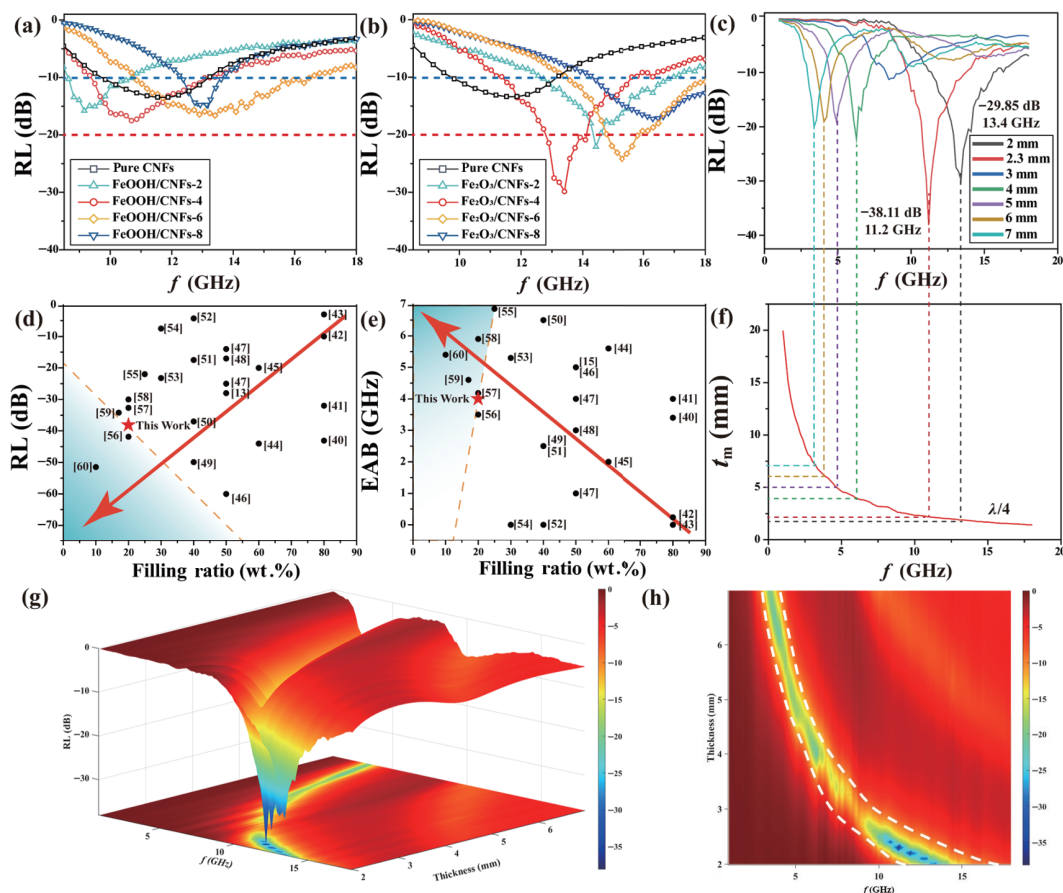
Figure 4 RL curves of (a) FeO(OH)/CNFs and (b) Fe$_2$O$_3$/CNFs with 20 wt.% filling ratio and 2 mm thickness. (c, g, h) RL of Fe$_2$O$_3$/CNFs-4 with different thicknesses. (d, e) RL value and EAB of typical Fe-based composite materials. (f) Simulation of the t_m of absorber versus f of Fe$_2$O$_3$/CNFs-4 under the $\lambda/4$ model.

performance may be severely impaired. Meanwhile, the RL$_{min}$ and EAB of FeOOH/CNFs are not strong enough, and it is necessary to further enrich the absorption mechanism. Under the same test condition, Fe$_2$O$_3$/CNFs possess stronger RL$_{min}$ values and wider EAB. As shown in Fig. 4(c), Fe$_2$O$_3$/CNFs-4 shows the best performance, the RL$_{min}$ can reach −29.8 dB, and the EAB can cover 4.6 GHz (11.2–15.8 GHz) at 2 mm; when the thickness increases to 2.3 mm, 4 GHz (9.8–13.8 GHz) of wide EAB and the −38.1 dB of strong RL$_{min}$ can be achieved. With the thickness increasing, the RL$_{min}$ gradually shifts to the low-frequency region, which is consistent with most of the previous work [39]. Figures 4(g) and 4(h) are 3D contour maps of RL values with different sample thicknesses and f. By adjusting the thickness, effective absorption of the EMW in 3–16 GHz can be met. In Figs. 4(d) and 4(e), and Table 1, following the arrow direction, the material can achieve stronger reflection loss and wider effective absorption bandwidth with a lower filling ratio. It is clear to see that the properties of Fe$_2$O$_3$/CNFs are close to even surpass some previously reported Fe-based composite materials, which strongly proved that the magnetic loss ability can be compensated and the EMW absorption performance can be effectively improved by rational microstructure design.

Figuer 4(f) investigates the f dependence on quarter-wavelength ($\lambda/4$) of Fe$_2$O$_3$/CNFs-4. When the t_m of the sample satisfies Eq. (1) below [61], the reflected wave will be significantly weakened or disappear.

$$t_m = nc / \left[(4f) \left(|\varepsilon_r| |\mu_r| \right)^{1/2} \right] \quad (1)$$

As the Fe$_2$O$_3$/CNFs-4 matching thickness increases, the RL$_{min}$ moves towards the low-frequency region, which obeys the matching condition of the $\lambda/4$ formula and is consistent with the
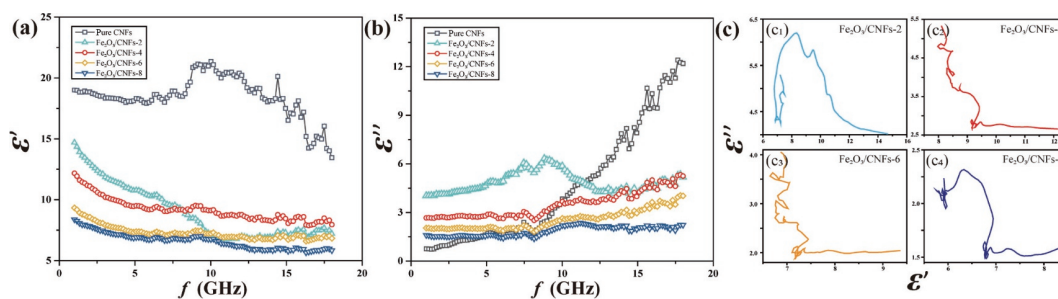
results reported in many works of literature [62, 63].

To investigate the EMW absorption enhancement mechanism of Fe$_2$O$_3$/CNFs composites, we tested the complex permittivity and complex permeability, which have an important effect on determining the EMW absorption ability [22]. Their real parts represent the store ability of dielectric and magnetic materials for EMW incident to their surfaces and their imaginary parts correspond to the loss capacity [64]. In general, the high permittivity will make the EMW seriously reflect on the surface of the material rather than absorb. As shown in Fig. 5, except for pure CNFs, the ε' of the complex permittivity of all four samples showed a decreasing trend with frequency increase. Among them, α-Fe$_2$O$_3$/CNFs-4 has a moderate ε', while α-Fe$_2$O$_3$/CNFs-6 and α-Fe$_2$O$_3$/CNFs-8 have the lowest ε' due to the high load of nanoparticles. There are two factors in the decrease of the dielectric constant. On the one hand, the surface defects formed by α-Fe$_2$O$_3$ nanoparticles gradually increased after calcination, affecting the integrity of CNFs conductive network. In the electromagnetic (EM) field, these defects act as the polarization center and significantly enhance the dipole polarization effect of materials [31]. On the other hand, since the presence of α-Fe$_2$O$_3$ greatly increases the resistivity (ρ) of the material, according to the free electron theory [29], $\varepsilon'' \approx 1/2\pi\varepsilon_0\rho f$ (where ε_0 represents the permeability of free space) with the more nanoparticles load, ρ value gradually increases, and ε'' gradually decreases, which is consistent with the four composites materials ε'' trend exhibited in Fig. 5(b).

Except for the positive effects on conduction loss and dipole polarization, the dielectric loss ability can also be regulated by interface polarization [31]. The irregularly stacked nanoparticles on the surface of the CNFs are not only conducive to the multi-reflections of EMW but also greatly increase the number of charge carriers between the contact surface of the materials. Besides, the

Table 1 Related literature about typical Fe-based carbon composites for EMW absorption (2–3mm)

Sample	Filling ratio (wt.%)	RL (dB)	EAB (GHz)	References
$Fe_3O_4/\alpha\text{-}Fe_2O_3$	80	−43.1	3.4	[40]
$SiO_2\text{-}B_2O_3\text{-}Al_2O_3\text{-}CaO\text{-}Fe_2O_3$	80	−32	4	[41]
$rGO/\alpha\text{-}Fe_2O_3$	80	−10	0	[42]
$\gamma\text{-}Fe_2O_3$	80	−3	0	[43]
$TiO_2/rGO/Fe_2O_3$(hexagonal-phase)	60	−44	5.6	[44]
$HMCS@f\text{-}\alpha\text{-}Fe_2O_3$	60	−20	2	[45]
$\alpha\text{-}Fe_2O_3@CoFe_2O_4$	50	−60	5	[46]
$H\text{-}Al\text{-}\gamma\text{-}Fe_2O_3$	50	−28	5	[13]
Fe_2O_3(rhombohedral)-inCNT	50	−25	4	[47]
$Fe/\alpha\text{-}Fe_2O_3$	50	−17	3	[48]
Fe_2O_3(rhombohedral)-outCNT	50	−14	1	[47]
$C@\alpha\text{-}Fe_2O_3@MWCNTs$	40	−49.9	2.5	[49]
$\alpha\text{-}Fe_2O_3/Fe_3O_4/Fe/C$	40	−37	6.5	[50]
$\gamma\text{-}Fe_2O_3$/carbon nanocomposites	40	−17.5	2.5	[51]
$\alpha\text{-}Fe_2O_3@SiO_2$	40	−4.3	0	[52]
$\alpha\text{-}Fe_2O_3@rGO$	30	−23.2	5.3	[53]
$\gamma\text{-}Fe_2O_3\text{-}MWNTs/PBO$	30	−7.5	0	[54]
$\alpha\text{-}Fe_2O_3/Fe_3O_4/PANI/MWCNT$	25	−22	7	[55]
$B(OH)_3/\alpha\text{-}Fe_2O_3\text{-}CMSs$	20	−41.83	3.5	[56]
$\alpha\text{-}Fe_2O_3/CNFs$	20	−38.1	4	This work
B/N co-doped $C@Fe_2O_3/Fe_3C/Fe\text{-}CNTs$	20	−32.7	4.18	[57]
$C\text{-}\gamma\text{-}Fe_2O_3@C\text{-}rGO$	20	−30	5.9	[58]
$\gamma\text{-}Fe_2O_3$/Porous rGO	17	−34.2	4.6	[59]
$\gamma\text{-}Fe_2O_3/CNTCM@CN$	10	−51.5	5.4	[60]

Figure 5 Electromagnetic parameters (a) ε', (b) ε'', and (c) Cole–Cole plots of $Fe_2O_3/CNFs$.

complete and uniform $\alpha\text{-}Fe_2O_3$ coating on the CNF surface cannot be ignored, and this kind of core–shell structure provides a large number of interfaces to the material. According to reports, the core–shell structure shows lower RL_{min} and wider EAB than one-component absorbers [29]. When the electric field is applied, a large amount of free charge is generated between the interfaces, resulting in strong interfacial polarization. The interfacial polarization can be effectively reflected by Cole–Cole curve. According to Debye theory, one semicircle in Cole–Cole curve can be used to describe a Debye relaxation process [30]. As shown in Fig. 5(c), the number of semicircles included in the Cole–Cole curve gradually increases with the nanoparticle load, which proves that the interface polarization inside the material is enhanced significantly. Compared with the Cole–Cole curve of pure CNFs in Fig. S10 in the ESM, it is difficult to improve interfacial polarization capability and enhance EMW absorption capacity by the cross-linking network structure of carbon fiber alone.

Figure 6 shows the details of permeability for $Fe_2O_3/CNFs$.

There is no significant difference in the μ' and μ'' values of the four composite materials, indicating that the increased $\alpha\text{-}Fe_2O_3$ load only plays the role of regulating the microstructure and adjusting the ratio of dielectric materials/magnetic materials in the composite materials. For $Fe_2O_3/CNFs$, with f increasing, the μ' value decreases from 1.10 to 0.87, mainly fluctuating around 1.0. The μ'' of $Fe_2O_3/CNFs$ is less than 0 after 7 GHz. The positive value of μ'' indicates that the incident electromagnetic energy is absorbed by the absorber and magnetic loss occurs in this frequency range. While a negative value of μ'' reveals the self-generated magnetic energy due to eddy current loss is different from the direction of the external magnetic field and radiates outward from the absorber [65]. The small fluctuation peaks in the figure are mostly generated by the eddy current effect and natural resonance, according to the known Eq. (2) [65]

$$C_0 = \mu''(\mu')^{-2}f^{-1} \tag{2}$$

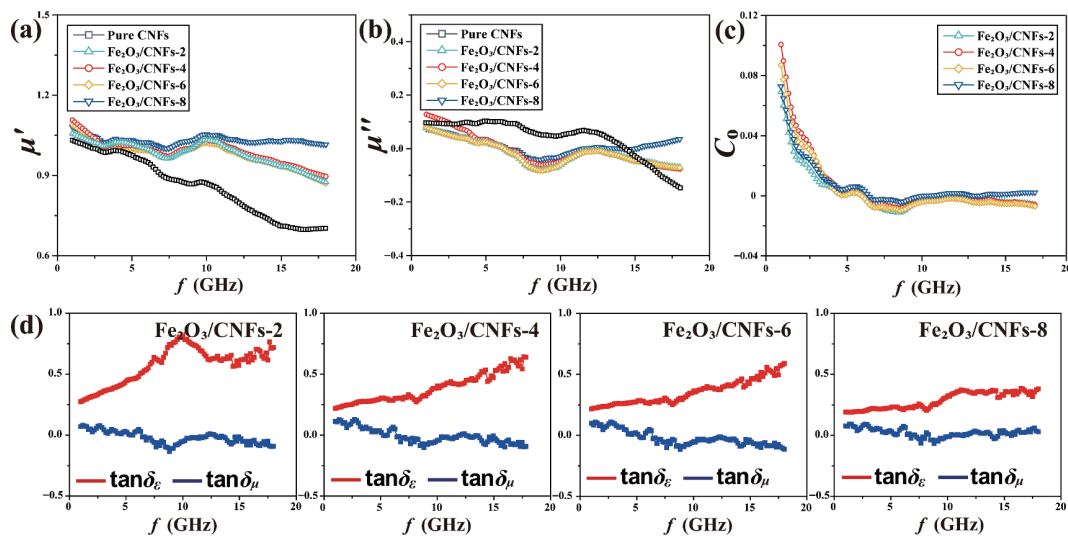If the changing trend of C_0 is not constant to f, the magnetic

Figure 6 Electromagnetic parameters (a) μ', (b) μ'', (c) C_0-f curves of the Fe$_2$O$_3$/CNFs, and (d) $\tan\delta_\varepsilon$ and $\tan\delta_\mu$.

loss of the material is caused by natural resonance, otherwise, it is caused by eddy current effects [66]. α-Fe$_2$O$_3$ belongs to paramagnetic materials, which can produce a weak eddy current loss with the change of magnetic flux. The magnetic loss trend of Fe$_2$O$_3$/CNFs shown in Fig. 6(c) illustrates that the composites are affected by natural resonance and eddy current loss in 1–7 and 7–18 GHz, respectively. Simultaneously, we measure the dielectric loss tangent angle ($\tan\delta_\varepsilon = \varepsilon''/\varepsilon'$) and magnetic loss tangent angle ($\tan\delta_\mu = \mu''/\mu'$) at 2 mm [30]. As shown in Fig. 6(d), $\tan\delta_\varepsilon$ is always larger than $\tan\delta_\mu$, indicating that the dielectric loss mechanism is the principal factor in the EMW absorption. Besides that the Fe$_2$O$_3$ nanoparticles on the CNFs show no significant contribution to $\tan\delta_\mu$, which is consistent with our design. Interestingly, although the increase of α-Fe$_2$O$_3$ failed to enhance the magnetic loss, it still effectively favors the complementarity between dielectric loss and magnetic loss, which is conducive to the impedance matching adjustment.

To further investigate the key factors for determining the EMW absorption performance, we consider the impedance matching values calculated by the equation $Z = |Z_{in}/Z_0|$. When Z is equal to 1, it means all of the EMW entering the material will be absorbed with no reflection. As shown in Fig. 7, the impedance matching of Fe$_2$O$_3$/CNFs-2 and Fe$_2$O$_3$/CNFs-4 with excellent performance tends to be 1, inferring that the input impedance is close to free space impedance. Fe$_2$O$_3$/CNFs-2 is closer to impedance matching so that EMW can be better absorbed by the material. However, due to the low load of Fe$_2$O$_3$ nanoparticles, the interface polarization and the multiple reflection loss between nanoparticles are weak, so the enhancement of the EMW absorption

performance and EAB is slightly inferior. Fe$_2$O$_3$/CNFs-4, whose impedance matching value is slightly higher than 1, has optimized interfacial polarization ability and rich reflection paths to achieve better absorption performance. The impedance matching values of Fe$_2$O$_3$/CNFs-6 and −8 are relatively high, which may be caused by the excessive Fe$_2$O$_3$ nanoparticle load. Under the same filling ratio, the content of nanoparticles is bigger, leading to the strong reflection of EMW rather than absorption on the composite surface. The above results show that the EMW absorbing materials, prepared by the *in-situ* transformation method, with properly hollow rice-grained α-Fe$_2$O$_3$ nanoparticles load and reasonable structural design, can achieve the purpose for adjusting impedance matching and enhancing the EMW absorption performance.

The possible EMW absorption mechanism in Fe$_2$O$_3$/CNFs can be inferred (Fig. 8). Firstly, due to the rich cross-linking network structure of CNFs, EMW experiences multi-reflections and scattering between CNFs. Under the action of the high-frequency alternating electromagnetic field, the 3D conductive network can convert electromagnetic energy into heat and dissipate it. Secondly, the overlapping and the hollow structure Fe$_2$O$_3$ can make the incident EMW reflect and absorb continuously many times, resulting in the EMW phase change, which can be canceled by other incident electromagnetic waves. Thirdly, the composite materials have rich heterogeneous interfaces, attaching to charge in the electromagnetic field and generating strong interfacial polarization. Finally, oxygen-containing functional groups and defects arising during acid treatment and calcination can be considered dipole centers, which spontaneously generate
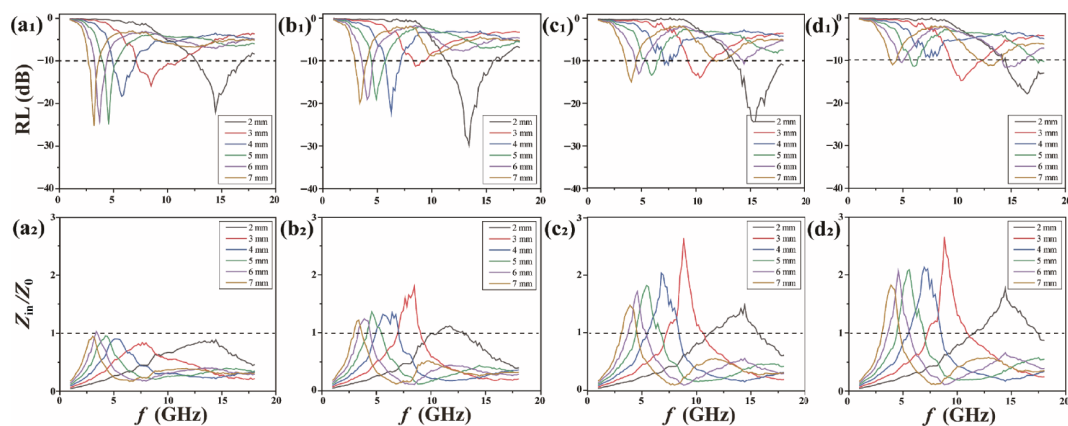

Figure 7 The normalized characteristic impedance Z_{in}/Z_0 of (a$_1$, a$_2$) Fe$_2$O$_3$/CNFs-2, (b$_1$, b$_2$) Fe$_2$O$_3$/CNFs-4, (c$_1$, c$_2$) Fe$_2$O$_3$/CNFs-6, and (d$_1$, d$_2$) Fe$_2$O$_3$/CNFs-8.
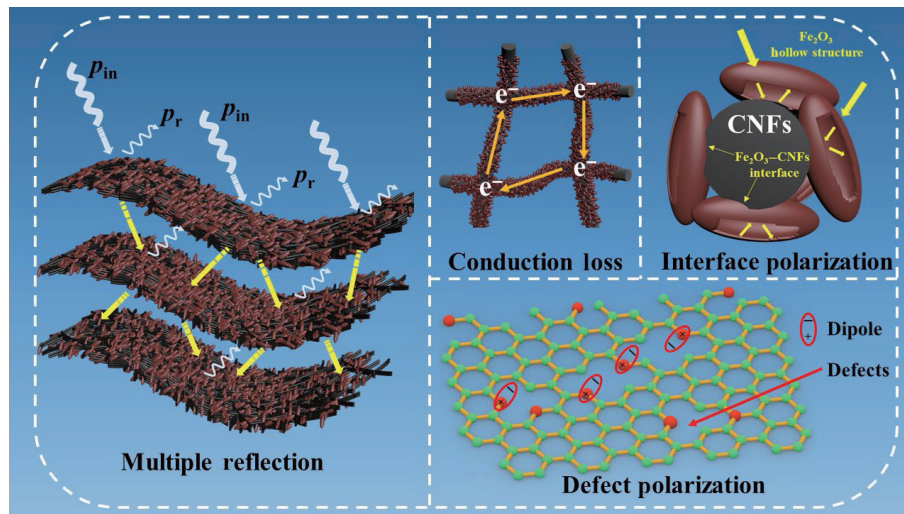
Figure 8 Schematic illustration of preparing Fe₂O₃/CNFs and possible EMW absorption mechanism.

asymmetric charge distributions and consume electromagnetic waves with rich polarization dipoles. To sum up, Fe₂O₃/CNFs composites have excellent EMW absorption properties due to their rational microstructural and rich internal synergistic mechanism.

3 Conclusions

In summary, hollow rice-grained Fe₂O₃ decorated on CNFs is constructed by a facile *in-situ* transformation method. According to the research design, we load the α-Fe₂O₃ nanoparticles with poor magnetic loss ability on pure CNFs to explore the influence of rational microstructure design on EMW absorption performance enhancement. The cross-linked network structure of CNFs not only provides abundant conduction loss but also solves the problems of agglomeration and uneven distribution of nanoparticles. The effective attenuation of EMW is realized by building rich cavity structures and complex reflection paths. The composite materials with excellent impedance matching were obtained by controlling the load of α-Fe₂O₃ nanoparticles. The results of the EMW absorption test show that a strong RL_{min} value of −38.1 dB at 2.3 mm and a wide EAB of 4.6 GHz at 2 mm were obtained with a filling ratio of 20 wt.%. We believe that the Fe₂O₃/CNFs nanocomposites provide a new perspective for the development of novel high-efficiency absorbing materials, and are very likely to achieve potentially practical application values.

Acknowledgements

References

[1] Aerts, S.; Vermeeren, G.; Van Den Bossche, M.; Aminzadeh, R.; Verloock, L.; Thielens, A.; Leroux, P.; Bergs, J.; Braem, B.; Philippron, A. et al. Lessons learned from a distributed RF-EMF sensor network. *Sensors* **2022**, *22*, 1715.

[2] Romeo, S.; Zeni, O.; Scarfì, M. R.; Poeta, L.; Lioi, M. B.; Sannino, A. Radiofrequency electromagnetic field exposure and apoptosis: A scoping review of *in vitro* studies on mammalian cells. *Int. J. Mol. Sci.* **2022**, *23*, 2322.

[3] Yang, H. H.; Zhang, Y. Y.; Wu, X. W.; Gan, P.; Luo, X. L.; Zhong,

[4] Cao, M. S.; Han, C.; Wang, X. X.; Zhang, M.; Zhang, Y. L.; Shu, J. C.; Yang, H. J.; Fang, X. Y.; Yuan, J. Graphene nanohybrids: Excellent electromagnetic properties for the absorbing and shielding of electromagnetic waves. *J. Mater. Chem. C* **2018**, *6*, 4586–4602.

[5] Song, Q.; Ye, F.; Kong, L.; Shen, Q. L.; Han, L. Y.; Feng, L.; Yu, G. J.; Pan, Y. A.; Li, H. J. Graphene and MXene nanomaterials: Toward high-performance electromagnetic wave absorption in gigahertz band range. *Adv. Funct. Mater.* **2020**, *30*, 2000475.

[6] Wang, Z.; Cheng, Z.; Fang, C. Q.; Hou, X. L.; Xie, L. Recent advances in MXenes composites for electromagnetic interference shielding and microwave absorption. *Compos. Part A Appl. Sci. Manuf.* **2020**, *136*, 105956.

[7] Zhang, Z. W.; Cai, Z. H.; Zhang, Y.; Peng, Y. L.; Wang, Z. Y.; Xia, L.; Ma, S. P.; Yin, Z. Z.; Wang, R. F.; Cao, Y. S. et al. The recent progress of MXene-based microwave absorption materials. *Carbon* **2021**, *174*, 484–499.

[8] Cheng, J.; Cai, L.; Shi, Y. Y.; Pan, F.; Dong, Y. Y.; Zhu, X. J.; Jiang, H. J.; Zhang, X.; Xiang, Z.; Lu, W. Polarization loss-enhanced honeycomb-like MoS₂ nanoflowers/undaria pinnatifida-derived porous carbon composites with high-efficient electromagnetic wave absorption. *Chem. Eng. J.* **2022**, *431*, 134284.

[9] Jin, C.; Chen, J. H.; Zhang, B. C.; Kong, L. W.; An, S. N.; He, Z. S.; Liu, J. L. Low-cost mmwave metallic waveguide based on multilayer integrated vertical-EBG structure and its application to slot array antenna design. *IEEE Trans. Antennas Propag.* **2022**, *70*, 2205–2213.

[10] Li, W.; Chen, X. Q.; Zhang, Z. L.; Wu, Z.; Yang, L.; Zou, Y. H. Ultralight and low-cost structural absorbers with enhanced microwave absorption performance based on sustainable waste biomass. *IEEE Trans. Antennas Propag.* **2022**, *70*, 401–409.

[11] Liu, Q. C.; Zi, Z. F.; Zhang, M.; Pang, A. B.; Dai, J. M.; Sun, Y. P. Enhanced microwave absorption properties of urchin-like Fe/α-Fe₂O₃ composite synthesized by a simple thermal oxidation. *Integr. Ferroelectr.* **2014**, *152*, 137–143.

[12] Xie, G. X.; Cheng, G. T.; Lv, T. Y.; Ma, J. Q.; Zhang, T. T.; Zhang, Y. R.; Yu, Y.; Jiang, L. L.; Wang, X. X.; Long, Y. Z. Electromagnetic properties and microwave absorption of electrospun Fe₂O₃-carbon composite nanofibers with particle-nanorod structure. *Nano* **2021**, *16*, 2150143.

[13] Zhang, H.; Xu, J.; Wang, S.; Liu, Q.; Kong, X. Constructing holey γ-Fe₂O₃ nanosheets with enhanced capability for microwave absorption. *Mater. Today Chem.* **2022**, *23*, 100690.

[14] Cheng, Y.; Chen, P.; Dong, S. T.; Zhang, Z. Y.; Guo, Y. H. Development of a porous iron-based magnetic absorber with

enhanced electromagnetic absorption performance. *J. Mater. Sci. Mater. Electron.* **2021**, *32*, 6799–6809.

[15] Fang, Y.; Wang, W. J.; Wang, S.; Hou, X. W.; Xue, W. D.; Zhao, R. A quantitative permittivity model for designing electromagnetic wave absorption materials with conduction loss: A case study with microwave-reduced graphene oxide. *Chem. Eng. J.* **2022**, *439*, 135672.

[16] Li, S. S.; Tang, X. W.; Zhang, Y. W.; Lan, Q. Q.; Hu, Z. W.; Li, L.; Zhang, N.; Ma, P. M.; Dong, W. F.; Tjiu, W. et al. Corrosion-resistant graphene-based magnetic composite foams for efficient electromagnetic absorption. *ACS Appl. Mater. Interfaces* **2022**, *14*, 8297–8310.

[17] Tian, K. H.; Huang, Y. N.; Zhang, C.; Shu, R. W.; Zhu, J. B.; Liu, Y.; Chen, Z. H.; Li, C.; Liu, X. W. *In-situ* synthesis of graphite carbon nitride nanotubes/cobalt@carbon with castor-fruit-like structure as high-efficiency electromagnetic wave absorbers. *J. Colloid Interface Sci.* **2022**, *620*, 454–464.

[18] Zhang, X. C.; Liu, M. J.; Xu, J.; Ouyang, Q. Y.; Zhu, C. L.; Zhang, X. L.; Zhang, X. T.; Chen, Y. J. Flexible and waterproof nitrogen-doped carbon nanotube arrays on cotton-derived carbon fiber for electromagnetic wave absorption and electric-thermal conversion. *Chem. Eng. J.* **2022**, *433*, 133794.

[19] Liu, X. D.; Huang, Y.; Zhao, X. X.; Yan, J.; Zong, M. Flexible N-doped carbon fibers decorated with Cu/Cu$_2$O particles for excellent electromagnetic wave absorption. *J. Colloid Interf Sci.* **2022**, *616*, 347–359.

[20] Ma, M. L.; Liao, Z. J.; Su, X. W.; Zheng, Q. X.; Liu, Y. Y.; Wang, Y.; Ma, Y.; Wan, F. Magnetic CoNi alloy particles embedded N-doped carbon fibers with polypyrrole for excellent electromagnetic wave absorption. *J. Colloid Interface Sci.* **2022**, *608*, 2203–2212.

[21] Zhao, K.; Ye, F.; Cheng, L. F.; Liu, R. Z.; Liang, J.; Li, X. Synthesis of embedded ZrC-SiC-C microspheres via carbothermal reduction for thermal stability and electromagnetic wave absorption. *Appl. Surf. Sci.* **2022**, *591*, 153105.

[22] Wang, R.; Sun, Q. L.; Gu, H.; Ye, W.; Yuan, G. Q.; Yang, Z. T.; Long, X. Y. Preparation and electromagnetic-wave-absorption properties of a nitrogen-doped carbon-supported iron(II, III) oxide composite. *J. Mater. Sci. Mater. Electron.* **2022**, *33*, 1383–1394.

[23] Shu, Y.; Zhao, T. K.; Li, X. H.; Yang, L.; Cao, S. Q.; Ahmad, A.; Jiang, T.; Luo, H. J.; Jing, Z. M.; Ui Ain, N. Surface plasmon resonance-enhanced dielectric polarization endows coral-like Co@CoO nanostructures with good electromagnetic wave absorption performance. *Appl. Surf. Sci.* **2022**, *585*, 152704.

[24] Guo, R.; Zheng, Q.; Wang, L. J.; Fan, Y. C.; Jiang, W. Porous N-doped Ni@SiO$_2$/graphene network: Three-dimensional hierarchical architecture for strong and broad electromagnetic wave absorption. *J. Mater. Sci. Technol.* **2022**, *106*, 108–117.

[25] Li, N.; Cao, M. H.; Hu, C. W. A simple approach to spherical nickel-carbon monoliths as light-weight microwave absorbers. *J. Mater. Chem.* **2012**, *22*, 18426–18432.

[26] Li, N.; Hu, C. W.; Cao, M. H. Enhanced microwave absorbing performance of CoNi alloy nanoparticles anchored on a spherical carbon monolith. *Phys. Chem. Chem. Phys.* **2013**, *15*, 7685–7689.

[27] Kong, B.; Liu, R.; Guo, J. H.; Lu, L.; Zhou, Q.; Zhao, Y. J. Tailoring micro/nano-fibers for biomedical applications. *Bioact. Mater.* **2023**, *19*, 328–347.

[28] Al-Dhahebi, A. M.; Ling, J.; Krishnan, S. G.; Yousefzadeh, M.; Elumalai, N. K.; Saheed, M. S. M.; Ramakrishna, S.; Jose, R. Electrospinning research and products: The road and the way forward. *Appl. Phys. Rev.* **2022**, *9*, 011319.

[29] Luo, H. L.; Zhang, Y.; Yang, Z. W.; Xiong, G. Y.; Wan, Y. Z. Constructing superior carbon-nanofiber-based composite microwave absorbers by engineering dispersion and loading of Fe$_3$O$_4$ nanoparticles on three-dimensional carbon nanofibers derived from bacterial cellulose. *Mater. Chem. Phys.* **2017**, *201*, 130–138.

[30] Liu, H.; Li, Y. J.; Yuan, M. W.; Sun, G. B.; Liao, Q. L.; Zhang, Y. Solid and macroporous Fe$_3$C/N-C nanofibers with enhanced electromagnetic wave absorbability. *Sci. Rep.* **2018**, *8*, 16832.

[31] Li, Y. J.; Yuan, M. W.; Liu, H. H.; Sun, G. B. *In situ* synthesis of CoFe$_2$O$_4$ nanocrystals decorated in mesoporous carbon nanofibers with enhanced electromagnetic performance. *J. Alloys Compd.* **2020**,

[32] Basavaraja, S.; Vijayanand, H.; Venkataraman, A.; Deshpande, U. P.; Shripathi, T. Characterization of γ-Fe$_2$O$_3$ nanoparticles synthesized through self-propagating combustion route. *Synth. React. Inorg. Metal-Org. Nano-Metal Chem.* **2007**, *37*, 409–412.

[33] Jia, C. J.; Sun, L. D.; Luo, F.; Han, X. D.; Heyderman, L. J.; Yan, Z. G.; Yan, C. H.; Zheng, K.; Zhang, Z.; Takano, M. et al. Large-scale synthesis of single-crystalline iron oxide magnetic nanorings. *J. Am. Chem. Soc.* **2008**, *130*, 16968–16977.

[34] Zhang, S. S.; Deng, P.; Yu, L. L.; Ni, Y.; Ling, C.; Zhu, Z. Y.; Liu, R. J. Fabrication and formation mechanism of hollow-structure supermagnetic α-Fe$_2$O$_3$/Fe$_3$O$_4$ heterogeneous nanospindles. *J. Inorg. Organomet. Polym. Mater.* **2022**, *32*, 2492–2501.

[35] Uhm, Y. R.; Kim, W. W.; Rhee, C. K. A study of synthesis and phase transition of nanofibrous Fe$_2$O$_3$ derived from hydrolysis of Fe nanopowders. *Scr. Mater.* **2004**, *50*, 561–564.

[36] Liu, H. H.; Li, Y. J.; Yuan, M. W.; Sun, G. B.; Li, H. F.; Ma, S. L.; Liao, Q. L.; Zhang, Y. *In situ* preparation of cobalt nanoparticles decorated in N-doped carbon nanofibers as excellent electromagnetic wave absorbers. *ACS Appl. Mater. Interfaces* **2018**, *10*, 22591–22601.

[37] Min, W. X.; Xu, D. W.; Chen, P.; Chen, G. Z.; Yu, Q.; Qiu, H. F.; Zhu, X. Y. Synthesis of novel hierarchical CoNi@NC hollow microspheres with enhanced microwave absorption performance. *J. Mater. Sci. Mater. Electron.* **2021**, *32*, 8000–8016.

[38] Xu, C.; Jin, D. Discussion on heat treatment of FeOOH. *Inf. Rec. Mater.* **1987**, *3*, 10–13,17.

[39] Han, Y. H.; Yuan, J.; Zhu, Y. H.; Wang, Q. Q.; Li, L.; Cao, M. S. Implantation of WSe$_2$ nanosheets into multi-walled carbon nanotubes for enhanced microwave absorption. *J. Colloid Interface Sci.* **2022**, *609*, 746–754.

[40] Ji, J. D.; Huang, Y.; Yin, J. H.; Zhao, X. C.; Cheng, X. W.; He, S. L.; Li, X.; He, J.; Liu, J. P. Synthesis and electromagnetic and microwave absorption properties of monodispersive Fe$_3$O$_4$/α-Fe$_2$O$_3$ composites. *ACS Appl. Nano Mater.* **2018**, *1*, 3935–3944.

[41] Wang, X. Y.; Huang, J. G.; Feng, H.; Li, J. F.; Pu, Z. D.; Yin, X. C. Facile preparation of the dendritic Fe$_3$O$_4$ with a core–shell microstructure in SiO$_2$-B$_2$O$_3$-Al$_2$O$_3$-CaO-Fe$_2$O$_3$ glass-ceramic system for enhanced microwave absorbing performance. *J. Alloys Compd.* **2021**, *877*, 160147.

[42] Zhang, H.; Xie, A. J.; Wang, C. P.; Wang, H. S.; Shen, Y. H.; Tian, X. Y. Novel rGO/α-Fe$_2$O$_3$ composite hydrogel: Synthesis, characterization and high performance of electromagnetic wave absorption. *J. Mater. Chem. A* **2013**, *1*, 8547–8552.

[43] Guo, C. Y.; Xia, F. Y.; Wang, Z.; Zhang, L.; Xi, L.; Zuo, Y. L. Flowerlike iron oxide nanostructures and their application in microwave absorption. *J. Alloys Compd.* **2015**, *631*, 183–191.

[44] Quan, B.; Xu, G. Y.; Li, D. R.; Liu, W.; Ji, G. B.; Du, Y. W. Incorporation of dielectric constituents to construct ternary heterojunction structures for high-efficiency electromagnetic response. *J. Colloid Interface Sci.* **2017**, *498*, 161–169.

[45] Ma, W. J.; Tang, C. H.; He, P.; Wu, X. H.; Cui, Z. K.; Lin, S.; Liu, X. Y.; Zhuang, Q. X. Morphology-controlled fabrication strategy of hollow mesoporous carbon spheres@f-Fe$_2$O$_3$ for microwave absorption and infrared stealth. *ACS Appl. Mater. Interfaces* **2022**, *14*, 34985–34996.

[46] Lv, H. L.; Liang, X. H.; Cheng, Y.; Zhang, H. Q.; Tang, D. M.; Zhang, B. S.; Ji, G. B.; Du, Y. W. Coin-like α-Fe$_2$O$_3$@CoFe$_2$O$_4$ core-shell composites with excellent electromagnetic absorption performance. *ACS Appl. Mater. Interfaces* **2015**, *7*, 4744–4750.

[47] Hu, H. H.; Zheng, Y.; Ren, K.; Wang, J. Y.; Zhang, Y. H.; Zhang, X. F.; Che, R. C.; Qin, G. W.; Jiang, Y. Position selective dielectric polarization enhancement in CNT based heterostructures for highly efficient microwave absorption. *Nanoscale* **2021**, *13*, 2324–2332.

[48] Jia, Z. R.; Wang, B. B.; Feng, A. L.; Liu, J. J.; Zhang, M.; Huang, Z. Y.; Wu, G. L. Development of spindle-cone shaped of Fe/α-Fe$_2$O$_3$ hybrids and their superior wideband electromagnetic absorption performance. *J. Alloys Compd.* **2019**, *799*, 216–223.

[49] Wang, L.; Yu, X. F.; Li, X.; Zhang, J.; Wang, M.; Che, R. C. Conductive-network enhanced microwave absorption performance from carbon coated defect-rich Fe$_2$O$_3$ anchored on multi-wall carbon

nanotubes. *Carbon* **2019**, *155*, 298–308.

[50] Chen, W. J.; Zhao, H.; Xu, B. B.; Jiang, Q. R.; Bao, S. S.; Jiang, Z. Y. Rational construction and microwave absorption properties of porous FeO$_x$/Fe/C composites. *J. Alloys Compd.* **2020**, *829*, 154519.

[51] Zhou, J. H.; He, J. P.; Wang, T.; Li, G. X.; Guo, Y. X.; Zhao, J. Q.; Ma, Y. O. Design of mesostructured gamma-Fe$_2$O$_3$/carbon nanocomposites for electromagnetic wave absorption applications. *J. Alloys Compd.* **2011**, *509*, 8211–8214.

[52] Fu, H. H.; Guo, Y.; Yu, J.; Shen, Z.; Zhao, J.; Xie, Y.; Ling, Y.; Ouyang, S.; Li, S. Q.; Zhang, W. Tuning the shell thickness of core–shell α-Fe$_2$O$_3$@SiO$_2$ nanoparticles to promote microwave absorption. *Chin. Chem. Lett.* **2022**, *33*, 957–962.

[53] Wang, L.; Zhang, J.; Wang, M.; Che, R. C. Hollow porous Fe$_2$O$_3$ microspheres wrapped by reduced graphene oxides with high-performance microwave absorption. *J. Mater. Chem. C* **2019**, *7*, 11167–11176.

[54] Chen, Y.; Liu, X.; Mao, X.; Zhuang, Q.; Xie, Z.; Han, Z. γ-Fe$_2$O$_3$-MWNT/poly(p-phenylenebenzobisoxazole) composites with excellent microwave absorption performance and thermal stability. *Nanoscale* **2014**, *6*, 6440–6447.

[55] Saeed, M. S.; Seyed-Yazdi, J.; Hekmatara, H. Fe$_2$O$_3$/Fe$_3$O$_4$/PANI/MWCNT nanocomposite with the optimum amount and uniform orientation of Fe$_2$O$_3$/Fe$_3$O$_4$ NPs in polyaniline for high microwave absorbing performance. *J. Alloys Compd.* **2020**, *843*, 156052.

[56] Zhong, B.; Wang, C. J.; Yu, Y. L.; Xia, L.; Wen, G. W. Facile fabrication of carbon microspheres decorated with B(OH)$_3$ and α-Fe$_2$O$_3$ nanoparticles: Superior microwave absorption. *J. Colloid Interface Sci.* **2017**, *505*, 402–409.

[57] Zhong, B.; Wang, C. J.; Wen, G. W.; Yu, Y. L.; Xia, L. Facile fabrication of boron and nitrogen co-doped carbon@Fe$_2$O$_3$/Fe$_3$C/Fe nanoparticle decorated carbon nanotubes three-dimensional structure with excellent microwave absorption properties. *Compos. Part B Eng.* **2018**, *132*, 141–150.

[58] Kou, X.; Zhao, Y. P.; Xu, L. J.; Kang, Z. L.; Wang, Y. C.; Zou, Z. Y.; Huang, P.; Wang, Q. F.; Su, G. H.; Yang, Y. et al. Controlled fabrication of core–shell γ-Fe$_2$O$_3$@C-reduced graphene oxide composites with tunable interfacial structure for highly efficient microwave absorption. *J. Colloid Interface Sci.* **2022**, *615*, 685–696.

[59] Wang, S.; Jiao, Q.; Liu, X.; Xu, Y.; Shi, Q.; Yue, S.; Zhao, Y.; Liu, H.; Feng, C.; Shi, D. Controllable synthesis of γ-Fe$_2$O$_3$ nanotube/porous rGO composites and their enhanced microwave absorption properties. *ACS Sustainable Chem. Eng.* **2019**, *7*, 7004–7013.

[60] Yu, X. F.; Zhang, Y.; Wang, L.; Xing, L. S.; You, W. B.; Liu, J. W.; Chen, G. Y.; Ding, G. Z.; Ding, J. Z.; Liu, X. H. et al. Improved microwave absorption performance of a multi-dimensional Fe$_2$O$_3$/CNTCM@CN assembly achieved by enhanced dielectric relaxation. *J. Mater. Chem. C* **2020**, *8*, 5715–5726.

[61] Qiao, J.; Zhang, X.; Xu, D. M.; Kong, L. X.; Lv, L. F.; Yang, F.; Wang, F. L.; Liu, W.; Liu, J. R. Design and synthesis of TiO$_2$/Co/carbon nanofibers with tunable and efficient electromagnetic absorption. *Chem. Eng. J.* **2020**, *380*, 122591.

[62] Qin, M.; Zhang, L. M.; Wu, H. J. Dielectric loss mechanism in electromagnetic wave absorbing materials. *Adv. Sci.* **2022**, *9*, 2105553.

[63] Sun, X. X.; Li, Y. B.; Huang, Y. X.; Cheng, Y. J.; Wang, S. S.; Yin, W. L. Achieving super broadband electromagnetic absorption by optimizing impedance match of rGO sponge metamaterials. *Adv. Funct. Mater.* **2022**, *32*, 2107508.

[64] Wang, Y. Q.; Zhao, H. B.; Cheng, J. B.; Liu, B. W.; Fu, Q.; Wang, Y. Z. Hierarchical Ti$_3$C$_2$T$_x$@ZnO hollow spheres with excellent microwave absorption inspired by the visual phenomenon of eyeless urchins. *Nano-Micro Lett.* **2022**, *14*, 76.

[65] Wang, Y. Q.; Wang, H. G.; Ye, J. H.; Shi, L. Y.; Feng, X. Magnetic CoFe alloy@C nanocomposites derived from ZnCo-MOF for electromagnetic wave absorption. *Chem. Eng. J.* **2020**, *383*, 123096.